



Article

Modeling Thermal Runaway Mechanisms and Pressure Dynamics in Prismatic Lithium-Ion Batteries

Mohammad Ayayda * , **Ralf Benger** , **Timo Reichrath**, **Kshitij Kasturia**, **Jacob Klink** and **Ines Hauer**

Research Center for Energy Storage Technologies, Clausthal University of Technology,
38678 Clausthal-Zellerfeld, Germany; ralf.benger@tu-clausthal.de (R.B.); timo.reichrath@tu-clausthal.de (T.R.);
ines.hauer@tu-clausthal.de (I.H.)

* Correspondence: mohammad.ayayda@tu-clausthal.de

Abstract: Lithium-ion batteries play a vital role in modern energy storage systems, being widely utilized in devices such as mobile phones, electric vehicles, and stationary energy units. One of the critical challenges with their use is the thermal runaway (TR), typically characterized by a sharp increase in internal pressure. A thorough understanding and accurate prediction of this behavior are crucial for improving the safety and reliability of these batteries. To achieve this, two new combined models were developed: one to simulate the thermal runaway and another to simulate the internal cell pressure. The thermal model tracks a chain of decomposition reactions that eventually lead to TR. At the same time, the pressure model simulates the proportional increase in pressure due to the evaporation of the electrolyte and the gases produced from the decomposition reactions. What sets this work apart is the validation of the pressure model through experimental data, specifically for prismatic lithium-ion cells using NMC chemistries with varying stoichiometries—NMC111 and NMC811. While the majority of the literature focuses on the simulation of temperature and pressure for cylindrical cells, studies addressing these aspects in prismatic cells are much less common. This article addresses this gap by conducting pressure validation experiments, which are hardly documented in the existing studies. Furthermore, the model's accuracy and flexibility are tested through two experiments, conducted under diverse conditions to ensure robust and adaptive predictions of cell behavior during failure scenarios.



Citation: Ayayda, M.; Benger, R.; Reichrath, T.; Kasturia, K.; Klink, J.; Hauer, I. Modeling Thermal Runaway Mechanisms and Pressure Dynamics in Prismatic Lithium-Ion Batteries. *Batteries* **2024**, *10*, 435. <https://doi.org/10.3390/batteries10120435>

Academic Editors: Fei Feng, Rui Ling, Yi Xie, Shunli Wang, Jinhao Meng and Jiale Xie

Received: 14 November 2024

Revised: 3 December 2024

Accepted: 4 December 2024

Published: 6 December 2024



Copyright: © 2024 by the authors. Licensee MDPI, Basel, Switzerland. This article is an open access article distributed under the terms and conditions of the Creative Commons Attribution (CC BY) license (<https://creativecommons.org/licenses/by/4.0/>).

1. Introduction

In recent years, the rise of electric vehicles has further intensified the demand for powerful and reliable energy storage systems. Lithium-ion batteries, renowned for their high energy density and efficiency, have become the cornerstone of this e-mobility revolution. Their ability to deliver substantial power with minimal weight, coupled with low self-discharge and negligible memory effects, makes them ideal for the rigorous demands of EVs. As a result, these batteries are now integral to the evolution of sustainable transportation [1]. Simultaneously, the global transition to renewable energy sources has underscored the need for efficient energy storage solutions. Lithium-ion technology stands out as the preferred option due to its cost-effectiveness and reliability, supporting a wide range of applications across industries. This dual role in both e-mobility and renewable energy integration illustrates the versatility and importance of lithium-ion batteries in today's energy landscape [2]. However, despite these benefits, Li-ion batteries also pose significant safety risks, particularly related to the phenomenon of thermal runaway (TR). TR can be triggered by various factors, such as thermal disturbances, overcharging, mechanical damage, or internal short circuits [3]. This phenomenon leads to uncontrolled temperature increases and a rapid rise in internal pressure due to the formation of gases from decomposition reactions and electrolyte evaporation [4–6]. If not promptly controlled in an adequate manner, these

processes can result in severe consequences, including fires or explosions [7]. Therefore, understanding the mechanism of thermal runaway is crucial for developing models that can replicate TR processes and predict associated pressure developments within the cell during a fault. By predicting thermal runaway, solutions can be developed to avoid its occurrence. For instance, calculating the cooling power required to prevent TR can serve as a basis for developing more effective thermal management systems. Thermal runaway consists of a sequence of reactions leading to the cell's self-heating and culminating in TR [8]. When the cell is triggered and its temperature exceeds 50 °C, the decomposition of the solid electrolyte interphase (SEI) initiates, producing gases such as C₂H₄, CO₂, O₂ and H₂ [9,10]. Further temperature increases expose the anode to the electrolyte, causing the formation of a new SEI layer, a process known as SEI regeneration. This process occurs in a temperature range of 120–250 °C and is associated with additional gas production, including C₃H₆, C₂H₂, and CH₄ [11,12]. The cell becomes unstable following the complete collapse of the separator, which leads to an internal short circuit. The melting point of the separator depends on the materials used. For instance, a multi-layer separator made from polypropylene (PP) and polyethylene (PE) will start to melt at around 127 °C for the PE layer and at approximately 165 °C for the PP layer [13–15]. Subsequent temperature increases lead to further decomposition of the electrolyte and cathode material, generating significant amounts of gases such as CO, O₂, and HF [9,10].

Correspondingly, the generation of gases and the evaporation of the electrolyte cause a rise in internal pressure within the cell. Figure 1 underscores the components responsible for pressure changes both before and after the venting event. Initially, the rise in pressure is due to the evaporation of the electrolyte, occurring prior to the onset of decomposition reactions. Subsequently, the pressure continues to increase as these decomposition reactions commence and more electrolyte evaporates [16]. When the pressure surpasses a critical threshold, the rupture disc bursts, opening the cell and releasing the gases, leading to first venting [5]. This gas outflow removes part of the heat from the cell, causing a temperature drop. The internal pressure falls to ambient levels but rises again rapidly due to gas generation from TR-driven decomposition reactions, as shown in Figure 1 and confirmed by Zhang et al. [17] and Mao et al. [18].

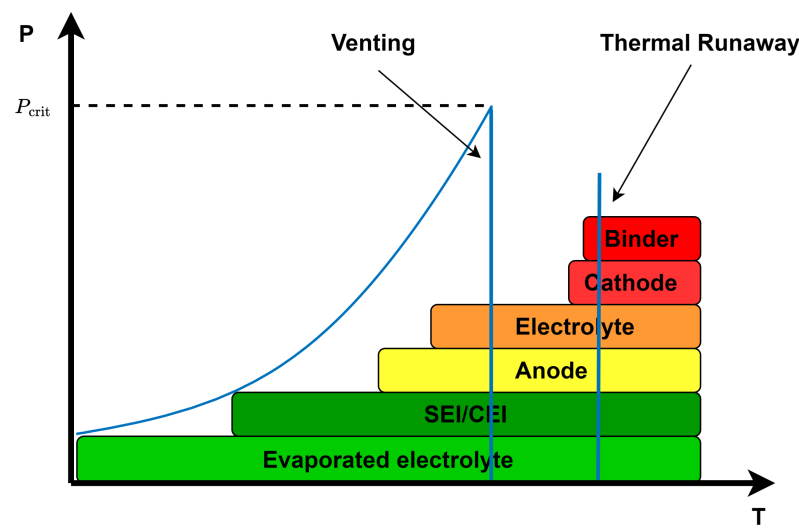


Figure 1. Illustration of the pressure increase in the cell and the contributing components. The diagram highlights the critical pressure point P_{crit} at which the cell opens and venting takes place, highlighting the elements responsible for pressure increases both prior to and following this event. Illustration style and insights are adapted from [19,20].

The current literature on the simulation and modeling of temperature and pressure during thermal runaway in prismatic cells is relatively sparse, with a predominant focus on cylindrical cells [21], as illustrated in Table 1. However, an exception to this trend is

the study conducted by Wang et al. [22], which examined a 27 Ah Lithium iron phosphate (LFP) prismatic cell subjected to thermal abuse. In their study, the cell was heated from the side with a 2000 W electric heater until thermal runaway was induced. The model developed by Wang et al. primarily addressed the simulation of temperature distributions, jet velocity, and mass loss during thermal abuse conditions. Another significant study is by Feng et al. [23], which comprehensively discussed the electrochemical-thermal behavior of cells under thermal abuse and successfully developed a model to simulate temperature and voltage profiles during TR. Their work was validated against experimental results from accelerating rate calorimeter (ARC) tests on a 25 Ah Lithium nickel manganese cobalt oxide (NMC) cell. However, none of these studies measured or described in detail the development of internal pressure in prismatic cells during TR.

Table 1. Overview of thermal and pressure modeling approaches for various cell chemistries and geometries found in the literature.

Cathode Chemistry	Geometry	Modeling Approach	Pressure Validation	Ref.
NMC	Cylindrical	Lumped	Yes	[21]
NMC	Cylindrical	Lumped	Yes	[18]
NMC	Cylindrical	Lumped	No	[24]
NMC	Cylindrical	3D	No	[17]
NCA	Cylindrical	Lumped	No	[25]
LFP	Prismatic	Lumped	No	[22]
NMC	Pouch	Lumped	No	[16]

In contrast to the current literature, the validation of the model results presented in this paper was conducted using data obtained from two distinct experimental setups that involved prismatic cells from the same manufacturer. These experiments utilized NMC111 and NMC811 cells, each with diverse capacities and subjected to a range of test conditions, including different states of charge (SoC), heating rates, heating orientations, initial temperatures, and other variables. By incorporating these diverse experimental conditions, the aim was to systematically validate the model's accuracy and reliability. This comprehensive approach was undertaken to demonstrate the model's flexibility and to ensure that it performs consistently and reliably under different operational scenarios, ultimately confirming its robustness and adaptability to a variety of conditions encountered in practical applications.

The primary contributions of this work include the development and integration of a novel combination of thermal and pressure models derived from the existing literature. Additionally, the use of NMC prismatic cells, which are commonly employed in the automotive industry, provided a relevant context for validating the simulation results. The study also highlights the versatility and reliability of the model by examining its performance under various experimental conditions and with different cathode stoichiometries. A significant focus of the paper is the validation of pressure data using experimental measurements, addressing a gap in the current literature, as shown in Table 1.

The remainder of this paper is structured as follows: Section 2 details the development strategy of the thermal and pressure models. This is followed by a description of the experiments conducted to validate the simulation results, presented in Section 3. Subsequently, Section 4 discusses the comparison between the model outputs and experimental data. Finally, the paper concludes with a summary in Section 5.

2. Model Development

The model is composed of interconnected thermal and pressure submodels, designed to simulate cell behavior during a thermal runaway event. The thermal submodel quantifies heat generation from decomposition reactions and potential short circuits, while the pressure submodel simulates internal pressure increases due to electrolyte evaporation and decomposition gas production as temperature rises.

The model is constructed as lumped, non-adiabatic frameworks, focusing on a single cell during thermal abuse conditions. Within this framework, the specific heat capacity and convection coefficient are assumed constant throughout the simulations. Additionally, the masses of the various cell components are estimated using measurements from similar cells reported in the literature.

2.1. Thermal Model

The developed thermal model, illustrated in Figure 2, comprises several interconnected submodules that collaboratively simulate the temperature profile of the cell. A key feature of the model is its adaptable external heating submodule, which can be configured to meet varying experimental requirements. This flexibility allows the heating to be specified either in terms of power (W) or heating rate (K/min).

The initiation of self-heating within the cell is represented in the decomposition submodule. This submodule simulates the decomposition reaction chain analogous to that observed in the actual cell. Once the separator fails, leading to an internal short circuit, the model simulates the heat generated from both the redox reaction between the anode and cathode and the heat produced from the internal short circuit. The quantification of the heat from the internal short circuit is based on established frameworks provided by previous studies, namely, the work of Feng et al. [26], Hong et al. [27], and Ren et al. [28].

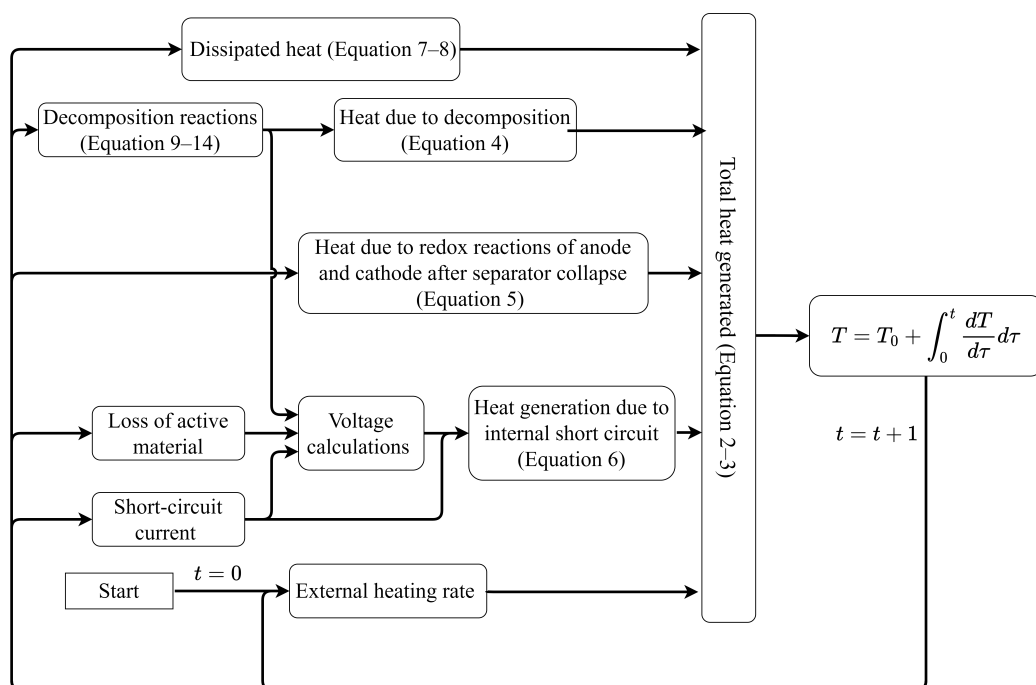


Figure 2. Flow chart of the thermal model considering heat generation within the cell, an external heat source, and heat dissipation (based on [23,26–28]).

2.1.1. Heat Generation in the Battery

The temperature T of the cell during TR can be calculated using [29]

$$T = T_0 + \int_0^t \frac{dT}{d\tau} d\tau \quad (1)$$

where T_0 is the initial temperature of the cell, and $\frac{dT}{d\tau}$ represents the rate of temperature change.

The rate of temperature change, $\frac{dT}{dt}$, can be determined using the following equation [23,30]:

$$\frac{dT}{dt} = \frac{\dot{Q}}{m_{\text{cell}}c_p} \quad (2)$$

where \dot{Q} is the total heat flow rate generated through various chemical reactions; m_{cell} is the total mass of the cell; and c_p is the specific heat capacity.

\dot{Q} is derived from several key sources, as shown in Equation (3):

$$\dot{Q} = \sum_z \dot{Q}_z + \dot{Q}_{\text{cat\&an}} + \dot{Q}_{\text{ISC}} - \dot{Q}_{\text{diss}} \quad (3)$$

where \dot{Q}_z represents the heat flow rate resulting from the decomposition reactions of the various components inside the cell: SEI, anode, electrolyte, and cathode; $\dot{Q}_{\text{cat\&an}}$ is the additional heat flow rate generated due to the rapid oxidation-reduction reaction after separator collapse, leading to direct contact between the anode and cathode. This contact prompts a complex and rapid oxidation-reduction reaction, attributed to “chemical crosstalk”, as proposed by Liu et al. [31] and Feng et al. [26]; \dot{Q}_{ISC} denotes the heat flow rate released due to short-circuit conditions; \dot{Q}_{diss} is the dissipated heat power into the environment. \dot{Q}_z is dependent on the decomposition rate of the reactants, $\frac{dc_z}{dt}$, as shown in Equation (4).

$$\dot{Q}_z = \Delta h_z \cdot m_z \cdot \frac{dc_z}{dt} \quad (4)$$

Δh_z represents the specific enthalpy of the reactants; and m_z denotes the mass of the components participating in the reaction. The mass utilized in calculating the heat generated from SEI decomposition is equivalent to the mass of the anode. Similarly, the mass employed in determining the heat generation from the cathode electrolyte interphase (CEI) decomposition corresponds to the mass of the cathode [21,24,26].

The heat released due to short-circuit conditions is determined by [26–28]

$$\dot{Q}_{\text{cat\&an}} = \frac{1}{\Delta t} \left(\Delta H_{\text{cat\&an}} - \int_0^t \dot{Q}_{\text{cat\&an}} d\tau \right) \quad (5)$$

$$\dot{Q}_{\text{ISC}} = \varsigma \left(\frac{V}{R_{\text{ISC}}} \right)^2 (R_{\text{cell}} + R_{\text{ISC}}) \quad (6)$$

Δt is the average short circuit time; $\Delta H_{\text{cat\&an}}$ is the total heat generation from oxidation-reduction reactions; ς is an efficiency factor used to correct for non-ohmic heat generation, as proposed by Coman et al. [32]; V is the voltage; R_{ISC} is the equivalent resistance in the resistor–capacitor circuit model; and R_{cell} is the internal resistance of the cell. Detailed calculations of voltage and resistance are based on the work of Feng et al. [26].

The heat dissipated to the environment due to convection \dot{Q}_{conv} and radiation \dot{Q}_{rad} is calculated using the following equations [33,34]:

$$\dot{Q}_{\text{conv}} = -h_{\text{conv}} A_{\text{cell}} (T - T_a) \quad (7)$$

$$\dot{Q}_{\text{rad}} = -\varepsilon \sigma A_{\text{cell}} (T^4 - T_a^4) \quad (8)$$

Here, h_{conv} is the convection heat transfer coefficient; A_{cell} is the surface area of the cell; ε is the surface emissivity; σ is the Stefan–Boltzmann constant; and T_a is the ambient temperature.

Table 2 presents the values of the parameters and constants utilized in the heat generation submodel.

Table 2. Parameters of the heat generation submodel for the tested prismatic cells [11,23,26,35].

Parameter	Symbol	Value	Unit
Specific heat capacity	c_p	1100	$\text{J kg}^{-1} \text{K}^{-1}$
Total mass of the NMC111 cell	m_{NMC111}	810	g
Total mass of the NMC811 cell	m_{NMC811}	900	g
Time constant	Δt	10	s
Total heat generation from redox reactions	$\Delta H_{\text{cat&an}}$	308	kJ
Efficiency factor	ζ	0.28	-
Heat transfer coefficient	h_{conv}	5	$\text{W m}^{-2} \text{K}^{-1}$
Surface area of the battery	A_{cell}	135	cm^2
Emissivity	ϵ	0.8	-
Stefan-Boltzmann constant	σ	5.67×10^{-8}	$\text{W m}^{-2} \text{K}^{-4}$

2.1.2. Reactions Kinetics

The reaction rate of the exothermal reactions involving the cell components can be described using the Arrhenius equation [32,36]:

$$\frac{dc_z}{dt} = A_z \cdot c_z^{n_{z,1}} \cdot (1 - c_z)^{n_{z,2}} \cdot \exp\left(-\frac{E_{a,z}}{R_0 T}\right) \quad (9)$$

where A_z is the frequency factor; c_z is the normalized concentration of the reactants; n_z is the reaction order; $E_{a,z}$ is the activation energy; and $R_0 = 8.314 \text{ J K}^{-1} \text{ mol}^{-1}$ is the ideal gas constant.

The normalized concentration c_z can be determined by

$$c_z = c_{z,0} - \int_0^t \frac{dc_z}{dt} d\tau \quad (10)$$

The regeneration of the SEI is proportional to the lithium-solvent reaction occurring at the anode. This regeneration can counterbalance the SEI decomposition, as described by [26]

$$\frac{dc_{\text{SEI}}}{dt} = \frac{dc_{\text{SEI-d}}}{dt} - \frac{dc_{\text{SEI-r}}}{dt} \quad (11)$$

$$\frac{dc_{\text{SEI-r}}}{dt} = K_{\text{SEI-r}} \cdot \frac{dc_{\text{an}}}{dt} \quad (12)$$

$\frac{dc_{\text{SEI-d}}}{dt}$ represents the SEI decomposition rate, which can be calculated using Equation (9). The term $\frac{dc_{\text{SEI-r}}}{dt}$ signifies the SEI regeneration rate, with $K_{\text{SEI-r}}$ as a proportional fitting factor, set to $K_{\text{SEI-r}} = 6$ [26].

The anode decomposition rate is extended with a correction factor that includes the regeneration of the SEI [37,38]:

$$\frac{dc_{\text{an}}}{dt} = A_{\text{an}} \cdot c_{\text{an}}^{n_{\text{an}}} \cdot \exp\left(-\frac{E_{a,\text{an}}}{RT}\right) \cdot \exp\left(-\frac{c_{\text{SEI}}}{c_{\text{SEI},0}}\right) \quad (13)$$

The values of the kinetic parameters for the decomposition submodel are listed in Table 3. It was assumed that the other cell properties remain unchanged in the cells investigated with two different cathode stoichiometries.

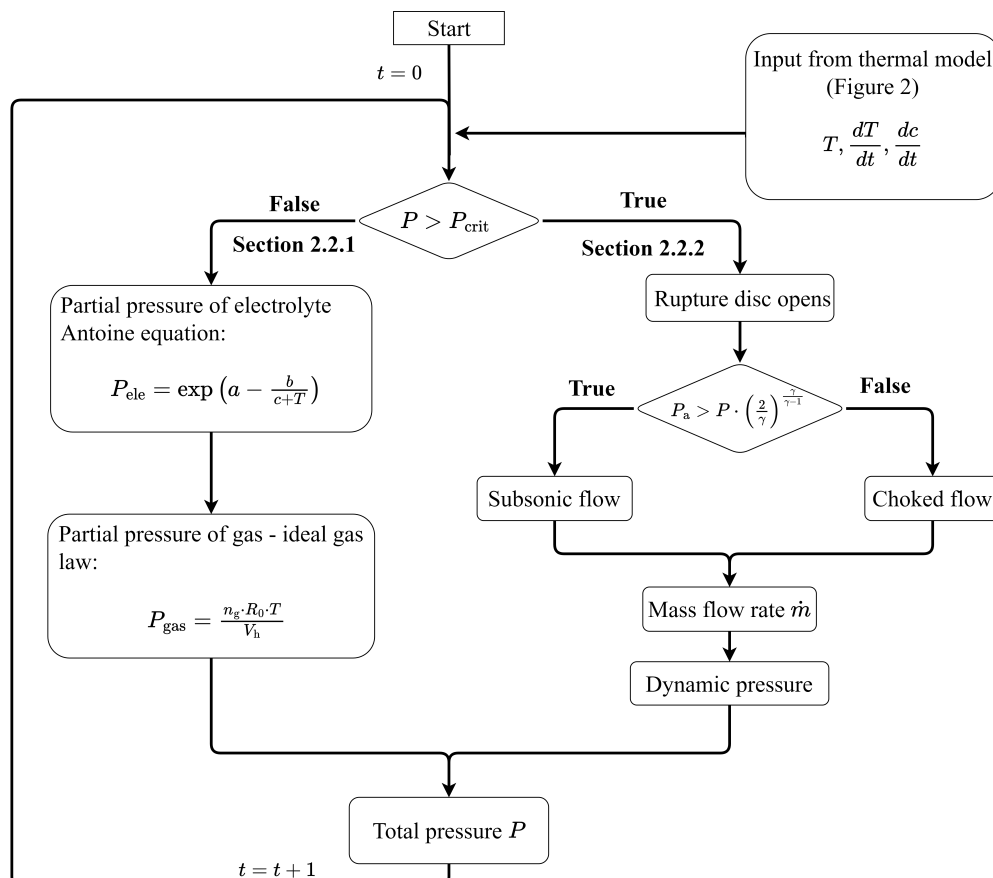
Table 3. Kinetic parameters for decomposition reactions.

z	Δh_z (J g ⁻¹)	$c_{z,0}$ (·)	$n_{z,1}(\cdot)$	$n_{z,2}(\cdot)$	A_z (s ⁻¹)	$E_{a,z}$ (J mol ⁻¹)	Ref.
SEI	257	0.15	5.5	0	5.32×10^{10}	9.64×10^4	[21]
CEI	257	0.15	5.5	0	1.21×10^{13}	1.03×10^5	[21]
Anode	1714	1	1	0	0.038 (T < 260 °C) 5 (T > 260 °C)	3.3×10^4	[26]
Separator	-190	1	1	0	1.5×10^{50}	4.2×10^5	[26]
Cathode _{NMC111}	154	0.04	1	1	2.25×10^{14}	7.9×10^5	[38]
Cathode _{NMC811}	1596	0.33	1	1	2.1×10^{17}	2.499×10^5	[39]
Binder	1500	1	1	0	1.077×10^{12}	1.5885×10^5	[35]
Electrolyte	800	1	1	0	3×10^{15}	1.7×10^5	[23]

2.2. Pressure and Venting Model

The pressure model is closely linked to the previously described thermal model, as it relies on temperature and decomposition reaction rates provided by the thermal model to calculate the pressure generated within the cell.

As illustrated in Figure 3, when the system's temperature increases due to generated or external heat, the internal pressure rises. This increase is primarily due to the evaporation of the electrolyte and the gases generated from decomposition reactions [16]. The internal pressure continues to rise with increased temperatures until a critical pressure threshold is reached, at which point the cell vents, releasing the accumulated gases and reducing the internal pressure [5]. Therefore, it is necessary to consider two distinct pressure regimes: the static pressure before cell venting and the dynamic pressure following the venting and gas outflow.

**Figure 3.** Flowchart for calculating pressure development in lithium-ion cells.

2.2.1. Internal Pressure Development Prior to Cell Opening

The initial increase in pressure is caused by the vaporized electrolyte according to He et al. [21], which can be calculated using the Antoine equation. The Antoine equation is a mathematical formula that relates the saturated vapor pressure of pure substances to temperature [40]:

$$P_{\text{ele}} = \exp\left(a - \frac{b}{c + T}\right) \quad (14)$$

where a , b , and c are fitting parameters used to align with pressure measurement data from experiments conducted before the onset of decomposition reactions.

The pressure increase due to gas production from decomposition reactions can be calculated using the ideal gas equation. He et al. [21] developed a simplified model to predict the pressure increase within the cell, taking into account gas generation primarily from the decomposition of the SEI and CEI layers. These decomposition reactions are the main contributors to internal gas production until the venting event. The partial pressure of the gas is calculated using Equation (15):

$$P_{\text{gas}} = \frac{n_{\text{gas}} R_0 T}{V_h} \quad (15)$$

where n_{gas} is the amount of generated gas in moles, R_0 is the universal gas constant, and V_h is the headspace volume of the cell, which accounts for 7% of the cell's total volume [5].

The quantity of gas generated, n_{gas} , is derived from Equation (16):

$$n_{\text{gas}} = \frac{m_{\text{gas,SEI}} + m_{\text{gas,CEI}}}{M_{\text{gas}}} \quad (16)$$

where $m_{\text{gas,SEI}}$ and $m_{\text{gas,CEI}}$ represent the mass of gas produced from SEI and CEI decomposition reactions, respectively, and M_{gas} is the molar mass of the generated gas.

The masses $m_{\text{gas,SEI}}$ and $m_{\text{gas,CEI}}$ can be determined by Equations (17)–(20):

$$c_{\text{gas,SEI}} = c_{\text{SEI},0} - c_{\text{SEI}} \quad (17)$$

$$c_{\text{gas,CEI}} = c_{\text{CEI},0} - c_{\text{CEI}} \quad (18)$$

$$m_{\text{gas,SEI}} = m_{\text{gas,SEI},0} \cdot c_{\text{gas,SEI}} \quad (19)$$

$$m_{\text{gas,CEI}} = m_{\text{gas,CEI},0} \cdot c_{\text{gas,CEI}} \quad (20)$$

where c_{SEI} and c_{CEI} are calculated using Equation (10); $m_{\text{gas,SEI},0}$ and $m_{\text{gas,CEI},0}$ represent the total masses of gases generated from SEI and CEI decomposition, accounting for 4.7% and 0.8% of the reactants' masses, respectively [21].

The overall internal pressure inside the cell is the sum of the pressure arising from the evaporated electrolyte and the pressure due to gas generated from decomposition reactions:

$$P = P_{\text{ele}} + P_{\text{gas}} \quad (21)$$

Table 4 shows the parameters for the pressure development in the cell prior to venting.

Table 4. Fitting and calculated parameters used to calculate the internal pressure in the cell prior to venting.

Parameter	Symbol	Value	Unit
Antoine constant	a	0.97 * for NMC111, 0.34 for NMC811	-
Antoine constant	b	150.49	K
Antoine constant	c	-279.85	K
Headspace volume	V_h	24.5	cm ³

* The value 0.97 for NMC111 takes into account preheating by 70 °C and the initial pressure value (see Section 3).

2.2.2. Dynamic Pressure Variation During the Venting Process

Wang et al. [22], Ostanel et al. [24], and Kong et al. [25] investigated the pressure dynamics following the venting after the rupture disc opens. They observed that the vapor–liquid equilibrium is disrupted upon venting, rendering the previously established equations in Section 2.2.1 invalid. The change in internal cell pressure can then be determined by differentiating the two pressure components in Equation (21) with respect to time:

$$\frac{dP}{dt} = \frac{dP_{\text{ele}}}{dt} + \frac{dP_{\text{gas}}}{dt} \quad (22)$$

When the rupture disc opens, the mass of electrolyte vapor, as well as the temperature in the cell, changes according to [17]:

$$\frac{dP_{\text{ele}}}{dt} = \frac{R_0 T}{M_{\text{ele}}} \cdot \frac{dm_{\text{ele}}}{dt} + \frac{m_{\text{ele}} R_0}{M_{\text{ele}} V_h} \cdot \frac{dT}{dt} \quad (23)$$

Here, m_{ele} stands for the electrolyte vapor mass in the cell void space; M_{ele} for the molar mass of the electrolyte vapor; and $\frac{dm_{\text{ele}}}{dt}$ is the change in electrolyte vapor mass per time.

$\frac{dm_{\text{ele}}}{dt}$ is calculated by [25]:

$$\frac{dm_{\text{ele}}}{dt} = -\varphi_{\text{ele}} \cdot \frac{dm_{\text{vent}}}{dt} \quad (24)$$

where φ_{ele} is the mass fraction of the electrolyte vapor in the vented mixture; and $\frac{dm_{\text{vent}}}{dt}$ is the mass flow rate of the vent gas. The calculation of $\frac{dm_{\text{vent}}}{dt}$ follows in Section 2.2.3. The integration of Equation (24) provides the instantaneous electrolyte vapor mass m_{ele} in the cell.

Similar calculations are used to simulate the dynamic change of the partial pressure of the generated gases.

$$\frac{dP_{\text{gas}}}{dt} = \frac{R_0 T}{M_{\text{gas}}} \cdot \frac{dm_{\text{gas}}}{dt} + \frac{m_{\text{gas}} R_0}{M_{\text{gas}} V_h} \cdot \frac{dT}{dt} \quad (25)$$

The change in the gas quantity in the cell $\frac{dm_{\text{gas}}}{dt}$ can be determined by the difference between the gas generated in the cell and the gas flow rate vented through the valve [17,25]:

$$\frac{dm_{\text{gas}}}{dt} = \left(m_z \frac{dc_z}{dt} \right) - \varphi_{\text{gas}} \frac{dm_{\text{vent}}}{dt} \quad (26)$$

where φ_{gas} is the mass fraction of the gas resulting from decomposition reactions in the vent gas. The mass fraction φ of the gases in the mass flow rate should lie within the range of 0 to 1. This fraction represents the proportion of the total mass flow rate attributable to the gaseous components. However, the sum of the mass fractions of the electrolyte vapor and generated gases will inherently be less than 1, as outlined in Table 5. This is because the model only considers the gas phase and does not account for the liquid portion of the electrolyte or solid particles, which are also part of the venting mass.

m_z is the mass of gas generated by decomposition reaction and is calculated as follows [17]:

$$m_z = X_i \cdot m_{\text{ventgas}} \quad (27)$$

where X_i is the ratio of the generated heat from the decomposition reaction to the total generated heat; m_{ventgas} is the total mass of the vent gas. The parameters used for calculating the dynamic pressure change are summarized in Table 5, while the ratio of gases produced by the decomposition reactions is detailed in Table 6.

Table 5. Parameters for calculating dynamic pressure changes (Equations (23)–(26)) [17,25].

Parameter	Symbol	Value	Unit
Molar mass of electrolyte vapor	M_{ele}	90.08	g mol^{-1}
Mass fraction of electrolyte vapor in vent gas	φ_{ele}	0.1	—
Mass fraction of generated gas in vent gas	φ_{gas}	0.2	—

Table 6. Values for the ratio of the generated heat from the decomposition reaction to the total generated heat [26].

z	X_i
SEI	0.03
Anode	0.28
Cathode	0.05
Electrolyte	0.14

2.2.3. Mass Flow Rate of Vent Gas

The mass flow rate $\frac{dm_{\text{vent}}}{dt}$ is calculated as follows, as proposed by Mao et al. [18]:

$$\frac{dm_{\text{vent}}}{dt} = \frac{u P_{\text{vent}} A_{\text{vent}} M_{\text{gas}}}{RT_{\text{vent}}} \quad (28)$$

Here, u represents the gas velocity; A_{vent} is the cross-sectional area of the burst opening, which is provided in the data sheet as $A_{\text{vent}} = 2.178 \text{ cm}^2$; P_{vent} is the pressure at the exit of the rupture disc opening in bar; and T_{vent} is the temperature at the exit of the opening. These parameters can be calculated using [5,24,25,41]

$$P_{\text{vent}} = \frac{P}{\left(1 + \frac{\gamma-1}{2} Ma^2\right)^{\frac{\gamma}{\gamma-1}}} \quad (29)$$

$$T_{\text{vent}} = \frac{T}{\left(1 + \frac{\gamma-1}{2} Ma^2\right)} \quad (30)$$

$$u = Ma \sqrt{\frac{\gamma R T_{\text{vent}}}{M_{\text{gas}}}} \quad (31)$$

$$Ma = \begin{cases} 0 & \text{if } P < P_{\text{crit}} \\ \sqrt{\frac{2}{\gamma-1} \left[\left(\frac{P}{P_a}\right)^{\frac{\gamma-1}{\gamma}} - 1 \right]} & \text{if } P_a > P \left[\frac{2}{\gamma+1} \right]^{\frac{\gamma-1}{\gamma}} \\ 1 & \text{if } P_a \leq P \left[\frac{2}{\gamma+1} \right]^{\frac{\gamma-1}{\gamma}} \end{cases} \quad (32)$$

P_a is the ambient pressure; γ is the heat capacity ratio $C_{p,\text{gas}} / C_{v,\text{gas}}$; and Ma is the Mach number, ranges between 0 and 1.

3. Experiments

The experimental validation of the thermal runaway model was carried out through abuse tests conducted with prismatic NMC111 and NMC811 cells. The experimental setups and conditions varied to evaluate the model's flexibility and applicability across different scenarios. To simulate real-world conditions, these tests were performed in a non-isolated test chamber. In all test scenarios presented in this paper, a constant heat ramp was used to trigger the thermal runaway of the cells.

As shown in Figure 4, the experiment setup of the cell consists of (1) a mounting and heating plate fixed on the sides of the cell, (2) temperature measuring sensors fixed on all

sides of the cell (T_1 – T_4) and on the rupture disc (labeled as “vent”) T_{V1} , (3) a temperature control sensor $T_{Control}$ directly connected to the cell to regulate heat input and maintain a consistent heating rate, and (4) a pressure sensor inserted through the seal pin.

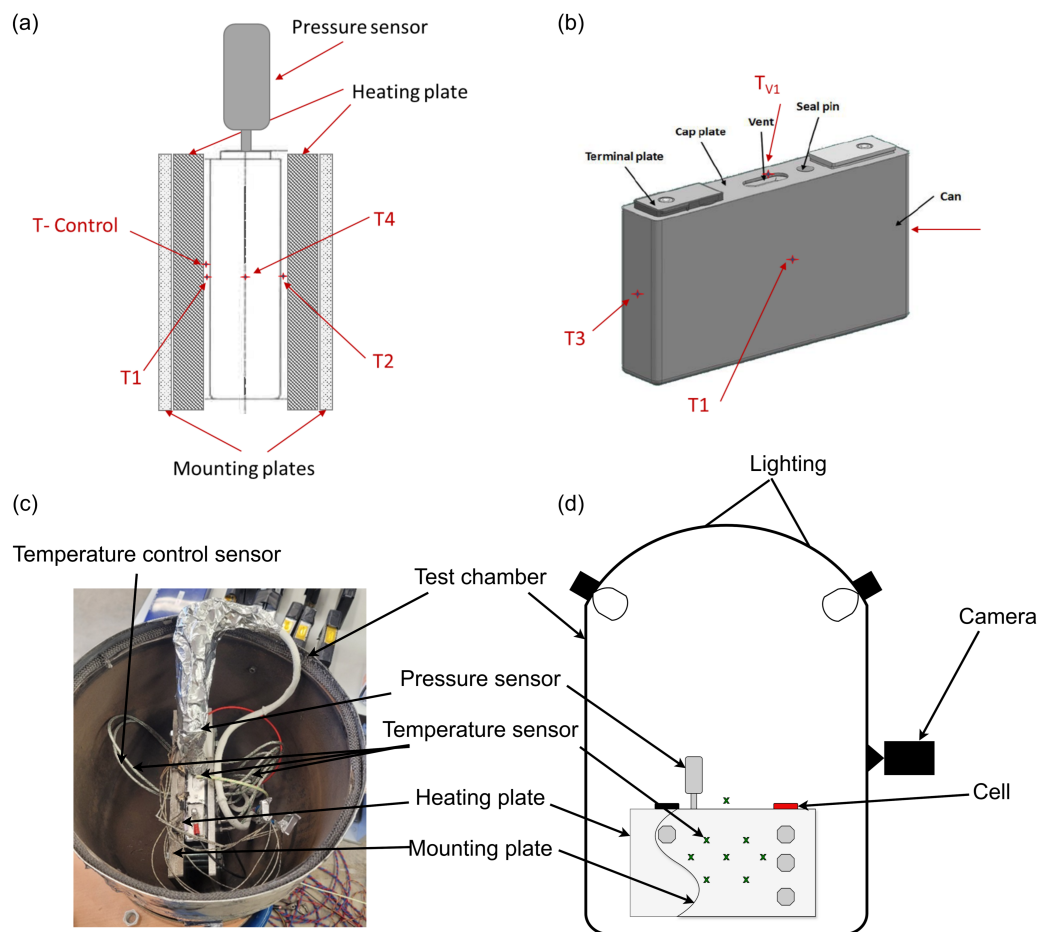


Figure 4. Experimental setup and test chamber configuration: (a) Side view of the battery cell illustrating the layout of the pressure sensor, temperature sensors, and heating plates; (b) tested prismatic cell with locations of temperature sensors and other key components; (c) real experimental chamber setup showcasing the arrangement of different temperature sensors and other elements; (d) schematic representation of the test chamber.

Conditions and Boundaries of the Experiments

The experimental conditions and boundaries are summarized in Table 7. In the first experiment, conducted by Orozav [19], an NMC111 cell with dimensions of 148 mm × 92 mm × 26.5 mm and a capacity of 37 Ah was utilized. While international abuse testing standards for lithium-ion batteries in electric vehicles typically recommend heating rates of 5–10 °C/min [42], a lower heating rate of 0.5 K/min was employed to ensure uniform temperature distribution by heating the cell from both sides. Prior to the commencement of the heating phase, the cell was preheated to 70 °C and maintained at this elevated temperature for a duration of 30 min. This preheating phase ensured a homogeneous temperature distribution and chemical stability, thereby establishing a controlled initial condition. Given the new condition of the cell and its specification allowing storage up to 70 °C, it is presumed that minimal or negligible decomposition reactions had occurred. As can be seen in Section 4.1.2, preheating caused a slight increase in pressure. The heating process was subsequently initiated with continuous monitoring of the cell temperature and internal pressure. This experimental setup aimed to validate the model's response to different initial conditions and heating profiles, demonstrating the model's flexibility under varying experimental scenarios.

In the second experiment, an NMC811 cell with dimensions of 148 mm × 94 mm × 26.5 mm and a capacity of 50 Ah was employed. The cell was preheated to 25 °C and maintained at this temperature for 30 min to ensure a homogeneous temperature distribution and chemical stability prior to the test. Following this stabilization period, the cell was subjected to asymmetric heating from one side at a rate of 10 K/min. This experimental condition aimed to assess the model's performance and simulation results under a different heating profile and configuration compared to the first experiment. Furthermore, this condition more closely simulates real-world scenarios where heat might propagate from an adjacent cell in a battery pack. Additionally, the high SOC of 95% represents a worst-case scenario for a commercially used cell. Continuous monitoring of the cell's temperature and internal pressure was conducted throughout the heating process, allowing for a comprehensive evaluation of the model under these specific experimental conditions.

Table 7. Comparison of the experimental conditions for the NMC111 and NMC811 experiments.

Parameter	NMC111	NMC811
Capacity	37 Ah	50 Ah
State of Charge (SoC)	80%	95%
Heating rate	0.5 K min ⁻¹	10 K min ⁻¹
Heating sides	Both sides	One side
Initial temperature	70 °C	25 °C

4. Results and Discussion

In this section, a comprehensive analysis is presented of the thermal and pressure dynamics occurring during thermal runaway events in the examined NMC111 and NMC811 lithium-ion cells. Controlled experiments and simulations were employed to evaluate the accuracy and reliability of the simulation models. Focus is placed on comparing temperature and pressure profiles across different experimental setups to determine the models' effectiveness in replicating the cell behavior during thermal instability events.

4.1. Discussion of NMC111 Experimental and Simulation Results

4.1.1. Temperature Profile of the NMC111

Figure 5 displays the temperature profile of the tested NMC111 cell, alongside the simulation results. As previously detailed, the cell was subjected to heating from an initial temperature of 70 °C at a rate of 0.5 K/min. The temperature increases gradually due to the low heating rate until the TR event occurs. During the experiment, a temperature drop was observed at the venting event. This drop is attributed to the dissipation of heat with the venting gas, where a part of the heat was carried away by the expelled gas, leading to a noticeable decrease in temperature. However, this temperature drop was not replicated in the simulation due to the model's assumption that the heat flow caused by venting is compensated by a higher external heating rate (ideal heating ramp, dT/dt is constant).

When comparing the experimental data with the simulation, it is evident that TR occurs eleven seconds earlier in the model than in the experiment. A notable difference is also observed in the maximum temperature during TR. The simulation shows a higher maximum temperature compared to the experimental data, with a discrepancy of 80 °C. Several factors could contribute to this difference: the simulated temperature is an average of readings from four temperature sensors (T_1 , T_2 , T_3 , and T_4), as shown in Figure 4, excluding the temperature at the rupture disc. Furthermore, the model does not consider the heat dissipation due to solid and fluid particles expelled during the second venting event of the TR. Exact comparison values are listed in Table 8.

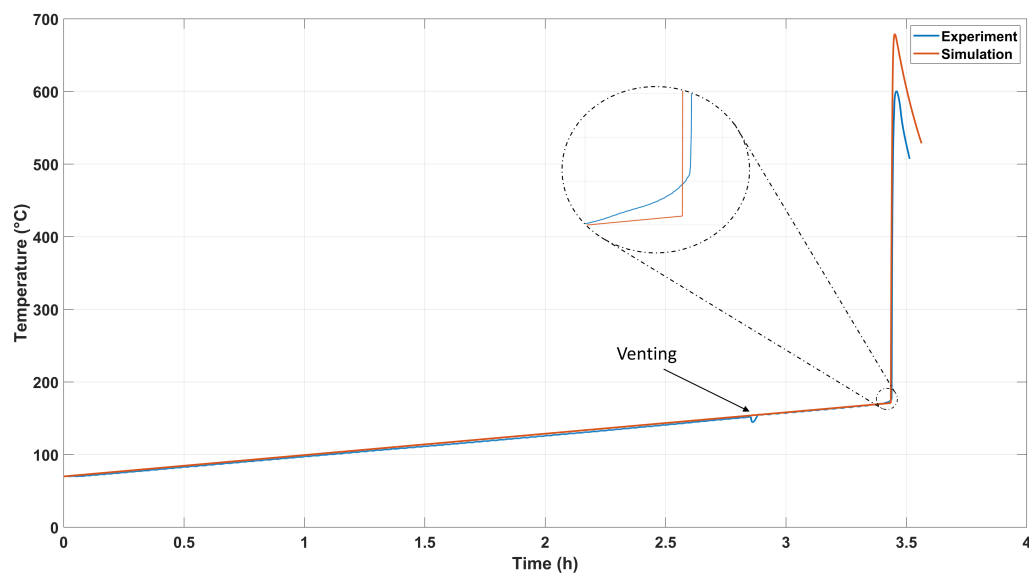


Figure 5. Comparison between measured and simulated temperature of the first experiment with NMC111 and a heating rate of 0.5 K/min (see parameters in Table 7).

Table 8. Comparison of the experimental data and simulation results of the experiments with NMC111.

Parameter	Experiment	Simulation
Time of TR t_{TR}	3 h and 26 min	3 h and 26 min
Maximal Temperature by TR T_{max}	600 °C	680 °C
Time of first venting t_{vent}	2 h and 51 min	2 h and 50 min
Temperature of first venting T_{vent}	152 °C	153.5 °C
Pressure increase by TR P_{TR}	N/A	0.74 bar

When evaluating the experimentally determined maximum temperature, great attention must be paid to the test conditions, as the position and dynamics of the temperature sensors can result in large differences, as Section 4.2.1 also shows. For this reason, results from different sources are often difficult to compare if the position and type of sensors and the test conditions are not exactly the same.

4.1.2. Pressure Profile of the NMC111

Figure 6 shows the pressure profile of the NMC111 cell during the experiment and its comparison with the simulation results. The initial pressure of 0.26 bar is caused by preheating the cell to 70 °C and maintaining this temperature for 30 min. Following this preheating phase, the temperature rise causes the pressure inside the cell to increase exponentially due to the evaporation of the electrolyte and the generation of gas until it reaches a critical pressure of 4.46 bar, prompting the cell to vent. In the experimental data, this critical pressure was reached after 2 h and 51 min at a temperature of 152 °C, whereas in the simulation, the predicted first venting occurred after 2 h and 50 min at a temperature of 153.5 °C, demonstrating a minimal discrepancy in both time and temperature.

Following the venting or opening of the cell, the pressure rapidly decreases to ambient levels due to the release of accumulated gases, which causes a corresponding drop in the temperature curve, as depicted in Figure 5. The pressure remains at ambient levels until the occurrence of TR. During the experimental procedure, the high temperatures during the TR process rendered the pressure sensor ineffective, preventing pressure measurements during this period. In contrast, the model predicts a significant pressure increase during TR, attributed to the rapid and substantial gas generation. The model indicates that the pressure increases again during TR, with a predicted rise of approximately 0.75 bar

due to the substantial amount of gas generated. This is similar to the results shown by Zhang et al. [17], Wang et al. [22], Ostaneck et al. [24], and Kong et al. [25].

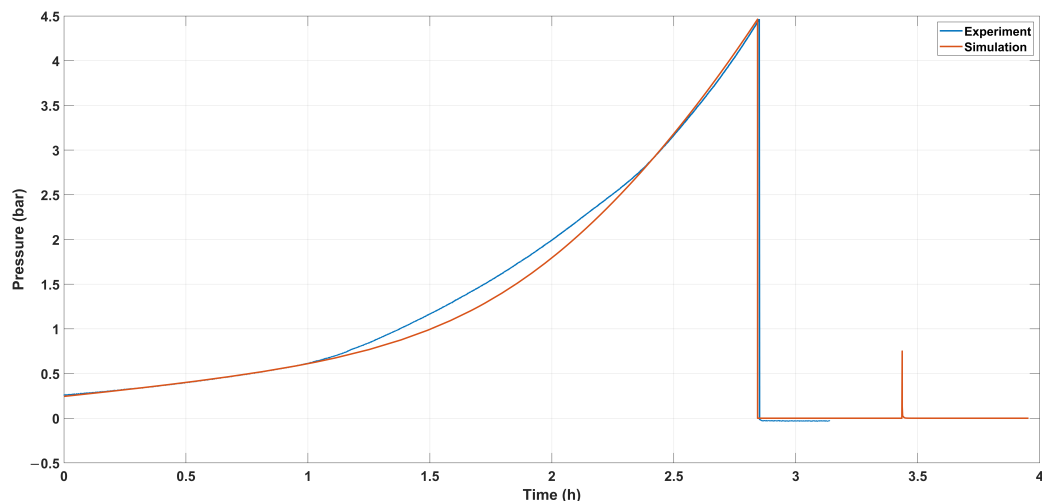


Figure 6. Comparison between measured and simulated pressure profiles of the NMC111 cell, highlighting pressure dynamics during thermal runaway, which were not measured experimentally.

The disparity in the pressure profiles between the experimental and simulated curves from 1 to 2.5 h can be attributed to several factors. Firstly, the 30-min preheating phase was not accounted for in the model, affecting the internal dynamics of the cell and leading to differences in the pressure build-up within this time interval. Additionally, small variations in experimental conditions, such as the rate of electrolyte evaporation and gas generation, may have contributed to the observed differences in pressure development between the two profiles. These discrepancies are considered acceptable given that many parameters in the model are empirically determined (see, for instance, Equation (14) concerning the Antoine parameters a , b , c and the mass fractions φ_{ele} and φ_{gas}). Moreover, the calculated root mean square error (RMSE) of 0.18 indicates a reasonably close fit between the simulated and experimental data. This RMSE value demonstrates the robustness of the model despite the simplifications and supports its reliability in predicting the pressure dynamics.

The results of the model compared to the experiment with NMC111 are listed in Table 8.

4.2. Discussion of NMC811 Experimental and Simulation Results

4.2.1. Temperature Profile of the NMC811

Figure 7 compares the simulated and measured temperature profiles of the NMC811 cell. The cell was heated from an initial temperature of 25 °C with a heating rate of 10 K/min from one side until TR occurred. Similar to the first experiment, the simulated temperature represents the average temperature recorded by various sensors positioned on the sides of the cell, as illustrated in Figure 4. The experimental data indicates an oscillating temperature curve due to the high-power heating plate used in this experiment, which was necessary to maintain the intended heating rate. As a result, no temperature drop due to the first venting was detected. Venting was observed shortly before the TR, occurring after approximately 22 min, as noted in Figure 8. This was confirmed through both visual observation during the experiment and pressure measurements.

A heating rate of 7 K/min is used in the model for the simulations, as the average temperature was simulated in the lumped thermal model. This means the heating rate reflects the temperature in the middle of the cell rather than at the sides, leading to differing internal temperature distributions. The non-linearity in the temperature profile is due to heating from one side and the thermal conductivity properties inside the cell.

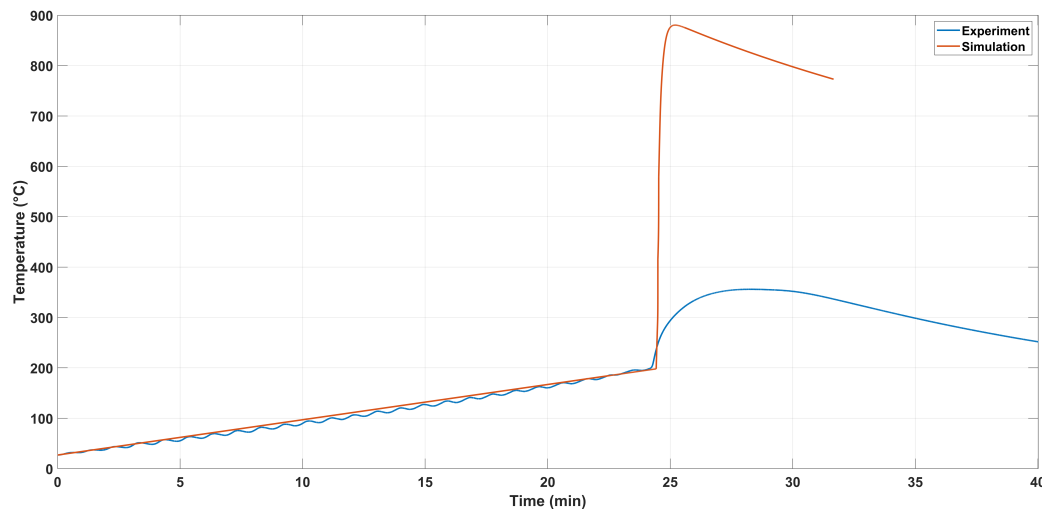


Figure 7. Comparison between measured and simulated temperature of abuse experiment with NMC811 and heating rate of 10 K/min.

The measured data show that TR was triggered 13 s earlier in the experiment compared to the simulation. The maximum temperature reached during TR in the simulation was 880 °C, whereas it was 350 °C in the measured data. This discrepancy can be attributed to the temperature sensors used, which likely have a larger diameter and a slower response time. Nevertheless, despite the high heating rate and the inhomogeneous temperature distribution in the cell, the time of the TR is well matched. The quality of the simulation is even better described by the pressure development, see Section 4.2.2.

4.2.2. Pressure Profile of the NMC811

As depicted in Figure 8, the internal pressure of the NMC811 cell increases exponentially with increasing temperature until it reaches 4.7 bar, at which point the rupture disc opens. Similar to the behavior observed in the NMC111 experiments, the pressure drops abruptly to 0 bar upon venting. In this particular experiment, a high-temperature-resistant sensor was utilized, recording a pressure of 1.6 bar during TR. The simulation, on the other hand, calculated a pressure of 1.25 bar.

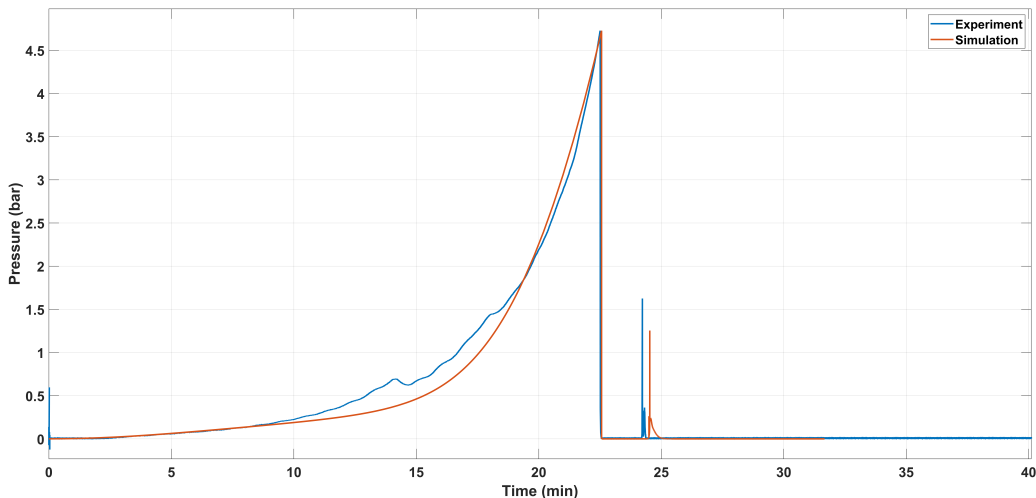


Figure 8. Comparison of measured and simulated pressure profiles for the NMC811 cell, highlighting the timing of venting events and pressure increase during thermal runaway.

The calculated RMSE for the pressure profiles is 0.23, suggesting a moderate level of discrepancy between the simulation and the experimental data. This RMSE value reflects

the simulation's fairly good performance in capturing the general trend and dynamics of pressure build-up within the cell. Notably, the simulation closely aligns with experimental observations, with the cell venting occurring only three seconds earlier than predicted. Additionally, the venting temperature was consistently captured at 185 °C in both the simulation and experimental scenarios.

The results of the model, as compared to the experiment with NMC811, are summarized in Table 9.

Table 9. Comparison of the experimental and simulation results of the experiments with NMC811.

Parameter	Experiment	Simulation
Time of TR (t_{TR})	24 min and 14 s	24 min and 27 s
Maximal Temperature during TR (T_{max})	350 °C	880 °C
Time of First Venting (t_{vent})	22 min and 30 s	22 min and 33 s
Temperature of First Venting (T_{vent})	185 °C	185 °C
Pressure during TR (P_{TR})	1.6 bar	1.25 bar

4.3. Additional Model Outputs

The model offers a range of additional outputs, providing insights into various thermal processes within the cell during a TR event. These outputs include the total generated heat, heat produced from the decomposition of different cell components, and dissipated heat, among others. Additionally, the model can simulate the cell voltage during TR events, offering a comprehensive understanding of the cell's thermal behavior and electrical response under extreme conditions.

One key focus, as shown in Figure 9, is the self-heating due to decomposition reactions, which begins with the breakdown of the SEI. With the increase in temperature, additional decomposition reactions are triggered, further contributing to self-heating and driving it toward a critical point where the separator begins to melt. The melting of the separator is an endothermic process, consuming energy and thus leading to a temporary decrease in apparent self-heating. However, these negative values during separator melting are not visible on the self-heating curve due to the limitations of the logarithmic scale used, a situation illustrated in Figure 9. Despite this, the heat input curve does reflect this phenomenon. It shows an increase in the supplied heat power to compensate for the energy absorbed by the separator's melting, ensuring the continued progression of thermal processes within the cell, maintaining the required heating rate of 7 K/min, as detailed in Section 4.2.1.

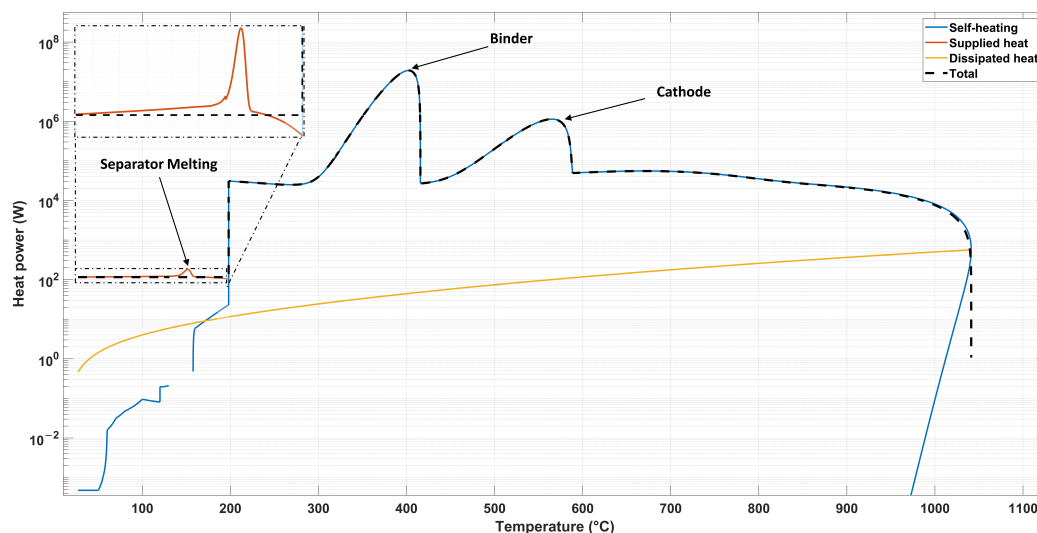


Figure 9. Illustration of simulated heat generation dynamics and associated dissipation processes in the NMC811 cell model.

The self-heating continues to escalate until the onset of thermal runaway (TR), where the generation power surges dramatically due to heat produced from redox reactions and potential short circuits, as described in Section 2.1. This rapid increase in thermal power is marked by two distinct peaks within the temperature range of 300–600 °C, which correspond to the decomposition of the binder and cathode materials, respectively. The heating power associated with these specific decomposition events is illustrated in Figure 10, offering a detailed view of the contributions from each component during these key temperature phases. The dissipated heat, calculated using Equations (7) and (8), shows a gradual increase with temperature elevation.

Figure 9 also clearly illustrates the model's constant total heat generation up until the onset of TR, correlating with the intended constant heating rate. The supplied heat, highlighted in the zoomed excerpt, is dynamically adjusted over time to compensate for dissipated heat and the energy consumed during separator melting, ensuring the heating rate remains consistent. After the separator melting, self-heating intensifies, reducing the amount of external power needed, which is reflected in the decline of the supplied power curve until it eventually ceases at TR. This detailed breakdown highlights the pivotal moment when self-heating exceeds dissipated heat, signifying that the cell will autonomously continue to increase in temperature, progressing toward TR, even in the absence of external heat input. This underscores the need for active cooling measures to prevent uncontrolled temperature rises and provides an estimation of the cooling power required to avert TR.

Figure 10 illustrates the simulated heat generation power and cumulative energy derived from decomposition reactions of various cell components at different temperatures. The figure identifies the key components responsible for heat generation and their corresponding temperature ranges. Figure 10a displays the heat power generated by each reaction, while Figure 10b shows the cumulative heat in joules. Self-heating initiates with the decomposition of the SEI, followed by anode decomposition starting around 120 °C. The decomposition of the electrolyte begins at approximately 140 °C, contributing significantly to heat generation, particularly dominant between 600 °C and 700 °C. At temperatures exceeding 200 °C, decomposition reactions from the cathode and binder further amplify the self-heating process, underscoring their roles in elevating cell temperatures during TR event.

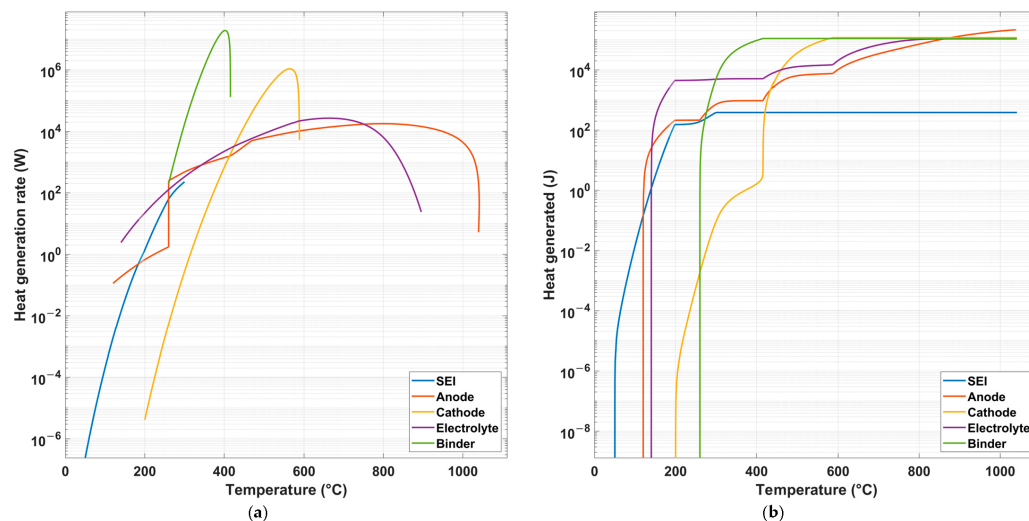


Figure 10. Simulated (a) heat generation power and (b) cumulative energy resulting from decomposition reactions of cell components, highlighting their roles across temperature ranges.

Additionally, the model can calculate the cell's voltage response to temperature changes during an abuse test, as depicted in Figure 11 for the example with the NMC811 cell. The cell starts with a state of charge (SoC) of 95% and an initial voltage of 4.12 V.

During the experiment, the voltage experiences a slight decrease of 0.01 V before the cell undergoes a short circuit. In contrast, the simulation indicates a voltage drop of 0.13 V before the short circuit. Following the onset of thermal runaway and the short circuit, the voltage sharply declines to 0 V but momentarily rebounds before ultimately falling to 0 V. Although the model does not exactly match the experimental data, it accurately captures the overall trend, including the fluctuation in the voltage observed experimentally. This behavior can be attributed to a decrease in internal cell resistance due to the temperature rise [43].

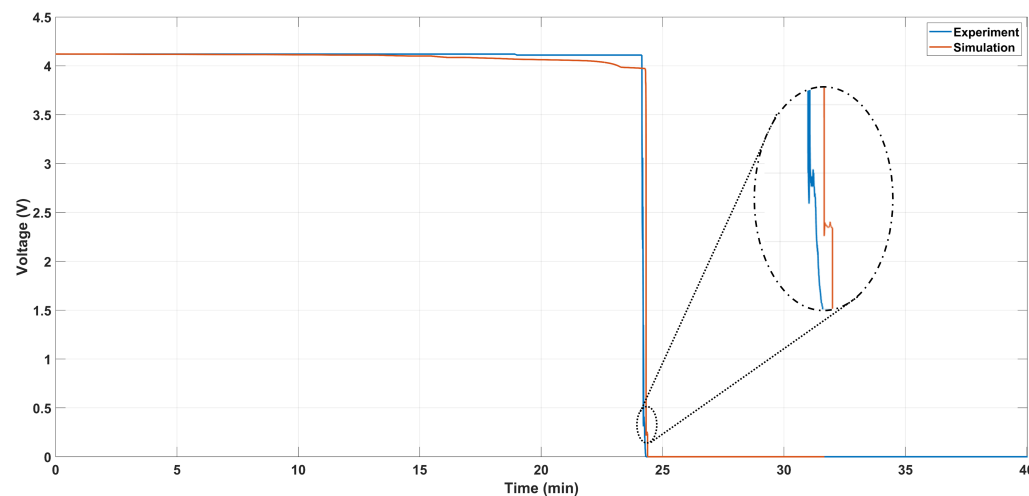


Figure 11. Simulated voltage response of an NMC811 cell during thermal abuse testing.

5. Conclusions

In this study, a comprehensive simulation model was developed to replicate the temperature and pressure development within prismatic lithium-ion cells, specifically focusing on NMC111 and NMC811 chemistries. The flexibility and accuracy of the model were rigorously evaluated under varied experimental conditions, including variations in heating rates, initial temperatures, and states of charge.

The thermal model incorporated into the simulation is based on the sequential decomposition reactions of key cell components, effectively capturing the heat production dynamics of a cell undergoing thermal abuse. This approach allowed for detailed replication of the cell's behavior during thermal runaway, considering both the heat generated internally and the heat dissipated to the environment.

Aligned with the thermal model, a pressure sub-model was developed to simulate the pressure rise inside the cell. This was attributed to both the evaporation of the electrolyte and the generation of gases from decomposition reactions. The simulation effectively modeled the critical pressure points leading to cell venting, accurately reflecting the experimental observations.

Upon validation, the model exhibited a slight discrepancy in the timing of thermal runaway and the maximum temperatures achieved compared to experimental data. Such differences have been attributed to the inherent variability in sensor responses and experimental conditions. Nonetheless, the overall trends observed in both temperature and pressure profiles were closely mirrored by the simulation results, demonstrating the robustness and reliability of the model.

Future enhancements could involve integrating sub-models like a cooling model to simulate thermal management strategies and extending the model to assess propagation phenomena within battery packs.

In conclusion, this simulation model offers a valuable tool for predicting the thermal and pressure behaviors of lithium-ion cells under various stress scenarios, enhancing the understanding of cell safety and reliability. Future work could refine the model by

including additional variables such as cell aging and the exploration of thermal runaway propagation among cells to further enhance its predictive capabilities.

Author Contributions: Conceptualization, M.A., T.R. and R.B.; methodology, M.A. and K.K.; software, M.A. and K.K.; validation, M.A. and T.R.; formal analysis, M.A.; investigation, M.A. and T.R.; resources, R.B.; data curation, M.A.; writing—original draft preparation, M.A.; writing—review and editing, M.A., R.B., J.K. and I.H.; visualization, M.A.; supervision, R.B. and I.H.; project administration, R.B.; funding acquisition, R.B. All authors have read and agreed to the published version of the manuscript.

Funding: Parts of this research were funded by the Federal Ministry for Economic Affairs and Energy of Germany in the project RiskBatt (project number: 03EI3010A). Other parts were funded by the Federal Ministry of Education and Research of Germany in the project VentBatt (project number: 03XP0535A).

Data Availability Statement: The data from the experiments are publicly accessible on the Zenodo platform, <https://doi.org/10.5281/zenodo.13981390>.

Acknowledgments: The authors acknowledge the support of the Open Access Publishing Fund of Clausthal University of Technology.

Conflicts of Interest: The authors declare no conflicts of interest.

Nomenclature

Variables

$\frac{dc}{dt}$	decomposition rate (s^{-1})
\dot{Q}	flow of heat rate (W)
$\frac{dm_{ele}}{dt}$	rate of mass change ($kg\ s^{-1}$)
$\frac{dm_{vent}}{dt}$	mass flow rate of the vent gas ($kg\ s^{-1}$)
$\frac{dP}{dt}$	pressure change rate ($Pa\ s^{-1}$)
$\frac{dT}{dt}$	rate of temperature change ($K\ s^{-1}$)
A_z	reaction frequency factor (s^{-1})
A_{cell}	cell dissipation area with ambient (m^2)
c	normalized concentration (—)
c_p	specific heat capacity ($J\ kg^{-1}\ K^{-1}$)
E_a	activation energy ($J\ mol^{-1}$)
h_{conv}	convection heat transfer coefficient ($W\ m^{-2}\ K^{-1}$)
M	molar mass ($kg\ mol^{-1}$)
m	mass (kg)
Ma	mach number (—)
n_z	reaction order (—)
P	pressure (Pa)
R	cell resistance (Ω)
R_0	gas constant ($J\ K^{-1}\ mol$)
T	temperature (K)
u	velocity ($m\ s^{-1}$)
V	voltage of the cell (V)
V_h	headspace volume (m^3)
X_i	ratio of the generated heat from z reaction to the total generated heat (—)

Greek

ΔH	enthalpy (J)
Δh	specific enthalpy ($J\ kg^{-1}$)
Δt	average short circuit time (s)
γ	heat capacity ratio (—)
σ	surface emissivity ($W\ m^{-2}\ K^{-4}$)
ε	surface emissivity (—)
φ	mass fraction in the vent gas (—)
ξ	efficiency factor used to correct the non-ohmic heat generation (—)

Subscripts

0	initial value
cat&an	oxidation and reduction reactions between cathode and anode
diss	heat dissipation
ISC	internal short circuit
a	ambient conditions
an	anode
ele	electrolyte
gas	parameters for generated gas from decomposition
SEI-r	SEI-regeneration
vent	vent gas
z	indicates the variable corresponds to reactant

Acronyms

ARC	accelerating rate calorimeter
CEI	cathode electrolyte interphase
LFP	lithium iron phosphate
NMC	lithium nickel manganese cobalt oxides
PE	Polyethylene
PP	Polypropylene
SEI	solid electrolyte interphase
SoC	state of charge

References

1. Şen, M.; Özcan, M.; Eker, Y. A Review on the Lithium-Ion Battery Problems Used in Electric Vehicles. *Next Sust.* **2024**, *3*, 100036. [[CrossRef](#)]
2. Ramadesigan, V.; Northrop, P.W.C.; De, S.; Santhanagopalan, S.; Braatz, R.D.; Subramanian, V.R. Modeling and Simulation of Lithium-Ion Batteries from a Systems Engineering Perspective. *J. Electrochem. Soc.* **2012**, *159*, R31. [[CrossRef](#)]
3. Christensen, P.A.; Anderson, P.A.; Harper, G.D.; Lambert, S.M.; Mrozik, W.; Rajaeifar, M.A.; Wise, M.S.; Heidrich, O. Risk Management over the Life Cycle of Lithium-Ion Batteries in Electric Vehicles. *Renew. Sustain. Energy Rev.* **2021**, *148*, 111240. [[CrossRef](#)]
4. Xu, C.; Fan, Z.; Zhang, M.; Wang, P.; Wang, H.; Jin, C.; Peng, Y.; Jiang, F.; Feng, X.; Ouyang, M. A Comparative Study of the Venting Gas of Lithium-Ion Batteries during Thermal Runaway Triggered by Various Methods. *Cell Rep. Phys. Sci.* **2023**, *4*, 101705. [[CrossRef](#)]
5. Coman, P.T.; Mátéfi-Tempfli, S.; Veje, C.T.; White, R.E. Modeling Vaporization, Gas Generation and Venting in Li-Ion Battery Cells with a Dimethyl Carbonate Electrolyte. *J. Electrochem. Soc.* **2017**, *164*, A1858. [[CrossRef](#)]
6. Klink, J.; Hebenbrock, A.; Grabow, J.; Orazov, N.; Nylén, U.; Benger, R.; Beck, H.P. Comparison of Model-Based and Sensor-Based Detection of Thermal Runaway in Li-Ion Battery Modules for Automotive Application. *Batteries* **2022**, *8*, 34. [[CrossRef](#)]
7. E, J.; Xiao, H.; Tian, S.; Huang, Y. A Comprehensive Review on Thermal Runaway Model of a Lithium-Ion Battery: Mechanism, Thermal, Mechanical, Propagation, Gas Venting and Combustion. *Renew. Energy* **2024**, *229*, 120762. [[CrossRef](#)]
8. Hu, X.; Gao, F.; Xiao, Y.; Wang, D.; Gao, Z.; Huang, Z.; Ren, S.; Jiang, N.; Wu, S. Advancements in the Safety of Lithium-Ion Battery: The Trigger, Consequence and Mitigation Method of Thermal Runaway. *Chem. Eng. J.* **2024**, *481*, 148450. [[CrossRef](#)]
9. Qiu, M.; Liu, J.; Cong, B.; Cui, Y. Research Progress in Thermal Runaway Vent Gas Characteristics of Li-Ion Battery. *Batteries* **2023**, *9*, 411. [[CrossRef](#)]
10. Wang, Q.; Mao, B.; Stolarov, S.I.; Sun, J. A Review of Lithium Ion Battery Failure Mechanisms and Fire Prevention Strategies. *Prog. Energy Combust. Sci.* **2019**, *73*, 95–131. [[CrossRef](#)]
11. Feng, X.; Ouyang, M.; Liu, X.; Lu, L.; Xia, Y.; He, X. Thermal Runaway Mechanism of Lithium Ion Battery for Electric Vehicles: A Review. *Energy Storage Mater.* **2018**, *10*, 246–267. [[CrossRef](#)]
12. Feng, X.; Sun, J.; Ouyang, M.; He, X.; Lu, L.; Han, X.; Fang, M.; Peng, H. Characterization of Large Format Lithium Ion Battery Exposed to Extremely High Temperature. *J. Power Sources* **2014**, *272*, 457–467. [[CrossRef](#)]
13. Li, Y.; Pu, H.; Wei, Y. Polypropylene/Polyethylene Multilayer Separators with Enhanced Thermal Stability for Lithium-Ion Battery via Multilayer Coextrusion. *Electrochim. Acta* **2018**, *264*, 140–149. [[CrossRef](#)]
14. Zhang, Q.K.; Zhang, X.Q.; Yuan, H.; Huang, J.Q. Thermally Stable and Nonflammable Electrolytes for Lithium Metal Batteries: Progress and Perspectives. *Small Sci.* **2021**, *1*, 2100058. [[CrossRef](#)]
15. Feng, X.; Zheng, S.; He, X.; Wang, L.; Wang, Y.; Ren, D.; Ouyang, M. Time Sequence Map for Interpreting the Thermal Runaway Mechanism of Lithium-Ion Batteries With $\text{LiNi}_x\text{Co}_y\text{Mn}_z\text{O}_2$ Cathode. *Front. Energy Res.* **2018**, *6*, 126. [[CrossRef](#)]
16. Cai, T.; Tran, V.; Stefanopoulou, A.G.; Siegel, J.B. Modeling Li-ion Battery First Venting Events Before Thermal Runaway. *IFAC-PapersOnLine* **2021**, *54*, 528–533. [[CrossRef](#)]
17. Zhang, P.; Lu, J.; Yang, K.; Chen, H.; Huang, Y. A 3D Simulation Model of Thermal Runaway in Li-ion Batteries Coupled Particles Ejection and Jet Flow. *J. Power Sources* **2023**, *580*, 233357. [[CrossRef](#)]

18. Mao, B.; Zhao, C.; Chen, H.; Wang, Q.; Sun, J. Experimental and Modeling Analysis of Jet Flow and Fire Dynamics of 18650-Type Lithium-Ion Battery. *Appl. Energy* **2021**, *281*, 116054. [[CrossRef](#)]
19. Orazov, N. Methode zur Zustandsbewertung Thermisch Beschädigter Lithium-Ionen-Zellen. Ph.D. Thesis, Clausthal University of Technology, Clausthal-Zellerfeld, Germany, 2024. [[CrossRef](#)]
20. Hebenbrock, A.; Orazov, N.; Benger, R.; Schade, W.; Hauer, I.; Turek, T. Innovative Early Detection of High-Temperature Abuse of Prismatic Cells and Post-Abuse Degradation Analysis Using Pressure and External Fiber Bragg Grating Sensors. *Batteries* **2024**, *10*, 92. [[CrossRef](#)]
21. He, C.X.; Yue, Q.L.; Chen, Q.; Zhao, T.S. Modeling Thermal Runaway of Lithium-Ion Batteries with a Venting Process. *Appl. Energy* **2022**, *327*, 120110. Simulation und venting. [[CrossRef](#)]
22. Wang, G.; Kong, D.; Ping, P.; Wen, J.; He, X.; Zhao, H.; He, X.; Peng, R.; Zhang, Y.; Dai, X. Revealing Particle Venting of Lithium-Ion Batteries during Thermal Runaway: A Multi-Scale Model toward Multiphase Process. *eTransportation* **2023**, *16*, 100237. [[CrossRef](#)]
23. Feng, X.; He, X.; Ouyang, M.; Lu, L.; Wu, P.; Kulp, C.; Prasser, S. Thermal Runaway Propagation Model for Designing a Safer Battery Pack with 25 Ah LiNi_xCo_yMn_zO₂ Large Format Lithium Ion Batter. *Appl. Energy* **2015**, *154*, 74–91. [[CrossRef](#)]
24. Ostanek, J.K.; Li, W.; Mukherjee, P.P.; Crompton, K.R.; Hacker, C. Simulating Onset and Evolution of Thermal Runaway in Li-ion Cells Using a Coupled Thermal and Venting Model. *Appl. Energy* **2020**, *268*, 114972. [[CrossRef](#)]
25. Kong, D.; Wang, G.; Ping, P.; Wen, J. A Coupled Conjugate Heat Transfer and CFD Model for the Thermal Runaway Evolution and Jet Fire of 18650 Lithium-Ion Battery under Thermal Abuse. *eTransportation* **2022**, *12*, 100157. [[CrossRef](#)]
26. Feng, X.; He, X.; Ouyang, M.; Wang, L.; Lu, L.; Ren, D.; Santhanagopalan, S. A Coupled Electrochemical-Thermal Failure Model for Predicting the Thermal Runaway Behavior of Lithium-Ion Batteries. *J. Electrochem. Soc.* **2018**, *165*, A3748. [[CrossRef](#)]
27. Hong, J.; Wang, Z.; Qu, C.; Zhou, Y.; Shan, T.; Zhang, J.; Hou, Y. Investigation on Overcharge-Caused Thermal Runaway of Lithium-Ion Batteries in Real-World Electric Vehicles. *Appl. Energy* **2022**, *321*, 119229. [[CrossRef](#)]
28. Ren, D.; Feng, X.; Lu, L.; Ouyang, M.; Zheng, S.; Li, J.; He, X. An Electrochemical-Thermal Coupled Overcharge-to-Thermal-Runaway Model for Lithium Ion Battery. *J. Power Sources* **2017**, *364*, 328–340. [[CrossRef](#)]
29. Ren, D.; Liu, X.; Feng, X.; Lu, L.; Ouyang, M.; Li, J.; He, X. Model-Based Thermal Runaway Prediction of Lithium-Ion Batteries from Kinetics Analysis of Cell Components. *Appl. Energy* **2018**, *228*, 633–644. [[CrossRef](#)]
30. Chen, J.; Ren, D.; Hsu, H.; Wang, L.; He, X.; Zhang, C.; Feng, X.; Ouyang, M. Investigating the Thermal Runaway Features of Lithium-Ion Batteries Using a Thermal Resistance Network Model. *Appl. Energy* **2021**, *295*, 117038. [[CrossRef](#)]
31. Liu, X.; Ren, D.; Hsu, H.; Feng, X.; Xu, G.L.; Zhuang, M.; Gao, H.; Lu, L.; Han, X.; Chu, Z.; et al. Thermal Runaway of Lithium-Ion Batteries without Internal Short Circuit. *Joule* **2018**, *2*, 2047–2064. [[CrossRef](#)]
32. Coman, P.T.; Darcy, E.C.; Veje, C.T.; White, R.E. Modelling Li-Ion Cell Thermal Runaway Triggered by an Internal Short Circuit Device Using an Efficiency Factor and Arrhenius Formulations. *J. Electrochem. Soc.* **2017**, *164*, A587. [[CrossRef](#)]
33. Kim, G.H.; Pesaran, A.; Spotnitz, R. A Three-Dimensional Thermal Abuse Model for Lithium-Ion Cells. *J. Power Sources* **2007**, *170*, 476–489. [[CrossRef](#)]
34. Jindal, P.; Kumar, B.S.; Bhattacharya, J. Coupled Electrochemical-Abuse-Heat-Transfer Model to Predict Thermal Runaway Propagation and Mitigation Strategy for an EV Battery Module. *J. Energy Storage* **2021**, *39*, 102619. [[CrossRef](#)]
35. Sun, X.; Xu, X.; Zhao, L.; Jin, H.; Cao, L.; Wang, H. Blocking Analysis of Thermal Runaway of a Lithium-Ion Battery under Local High Temperature Based on the Material Stability and Heat Dissipation Coefficient. *Ionics* **2021**, *27*, 107–122. [[CrossRef](#)]
36. Mishra, D.; Jain, A. Multi-Mode Heat Transfer Simulations of the Onset and Propagation of Thermal Runaway in a Pack of Cylindrical Li-Ion Cells. *J. Electrochem. Soc.* **2021**, *168*, 020504. [[CrossRef](#)]
37. Peng, P.; Jiang, F. Thermal Safety of Lithium-Ion Batteries with Various Cathode Materials: A Numerical Study. *Int. J. Heat Mass Transf.* **2016**, *103*, 1008–1016. [[CrossRef](#)]
38. Kong, D.; Wang, G.; Ping, P.; Wen, J. Numerical Investigation of Thermal Runaway Behavior of Lithium-Ion Batteries with Different Battery Materials and Heating Conditions. *Appl. Therm. Eng.* **2021**, *189*, 116661. [[CrossRef](#)]
39. Nguyen, T.T.D. Understanding and Modelling the Thermal Runaway of Li-Ion Batteries. Ph.D. Thesis, Université de Picardie Jules Verne, Amiens, France, 2021.
40. Behr, A.; Agar, D.W.; Jörissen, J.; Vorholt, A.J. (Eds.) Physikalisch-chemische Grundlagen I: Gleichgewichte und Thermodynamik. In *Einführung in die Technische Chemie*; Springer: Berlin/Heidelberg, Germany, 2016; pp. 29–42. [[CrossRef](#)]
41. Birch, A.D.; Hughes, D.J.; Swaffield, F. Velocity Decay of High Pressure Jets. *Combust. Sci. Technol.* **1987**, *52*, 161–171. [[CrossRef](#)]
42. Ruiz, V.; Pfrang, A.; Kriston, A.; Omar, N.; Van den Bossche, P.; Boon-Brett, L. A Review of International Abuse Testing Standards and Regulations for Lithium Ion Batteries in Electric and Hybrid Electric Vehicles. *Renew. Sustain. Energy Rev.* **2018**, *81*, 1427–1452. [[CrossRef](#)]
43. Long, M.K.; Liu, S.; Zhang, G. A Novel Method for Simultaneous Triggering and in Situ Sensing of Internal Short Circuit in Lithium-Ion Cells. *Energy Adv.* **2023**, *2*, 2018–2028. [[CrossRef](#)]

Disclaimer/Publisher's Note: The statements, opinions and data contained in all publications are solely those of the individual author(s) and contributor(s) and not of MDPI and/or the editor(s). MDPI and/or the editor(s) disclaim responsibility for any injury to people or property resulting from any ideas, methods, instructions or products referred to in the content.